Nano Research
2023, 16(7): 9983–9989
ISSN 1998-0124 CN 11-5974/O4
https://doi.org/10.1007/s12274-023-5487-3

Research Article

$CsPbBr_3$-DMSO merged perovskite micro-bricks for efficient X-ray detection

Tongyu Shi[1,2,§], Wenjun Liu[1,3,§], Jiongtao Zhu[1], Xiongsheng Fan[1], Zhengyu Zhang[1], Xingchen He[1], Rui He[1], Jiahong Wang[1,2], Kezhen Chen[1,2], Yongshuai Ge[1,2], Xiangming Sun[4], Yanliang Liu[1,2] (✉), Paul K. Chu[5], and Xue-Feng Yu[1,2] (✉)

[1] *Shenzhen Institute of Advanced Technology, Chinese Academy of Sciences, Shenzhen 518055, China*
[2] *University of Chinese Academy of Sciences, Beijing 100049, China*
[3] *Nano Science and Technology Institute, University of Science and Technology of China, Suzhou 215123, China*
[4] *Key Laboratory of Quark and Lepton Physics (MOE), Central China Normal University, Wuhan 430079, China*
[5] *Department of Physics, Department of Materials Science and Engineering, and Department of Biomedical Engineering, City University of Hong Kong, Hong Kong 999077, China*
[§] *Tongyu Shi and Wenjun Liu contributed equally to this work.*

Received: 30 October 2022 / **Revised:** 19 December 2022 / **Accepted:** 9 January 2023

ABSTRACT

Inorganic perovskite wafers with good stability and adjustable sizes are promising in X-ray detection but the high synthetic temperature is a hindrance. Herein, dimethyl sulfoxide (DMSO) is used to prepare the $CsPbBr_3$ micro-bricks powder at room temperature. The $CsPbBr_3$ powder has a cubic shape with few crystal defects, small charge trap density, and high crystallinity. A trace amount of DMSO attaches to the surface of the $CsPbBr_3$ micro-bricks via Pb–O bonding, forming the $CsPbBr_3$-DMSO adduct. During hot isostatic processing, the released DMSO vapor merges the $CsPbBr_3$ micro-bricks, producing a compact and dense $CsPbBr_3$ wafer with minimized grain boundaries and excellent charge transport properties. The $CsPbBr_3$ wafer shows a large mobility-lifetime (μτ) product of 5.16×10^{-4} $cm^2 \cdot V^{-1}$, high sensitivity of 14,430 $\mu C \cdot Gy_{air}^{-1} \cdot cm^{-2}$, low detection limit of 564 $nGy_{air} \cdot s^{-1}$, as well as robust stability in X-ray detection. The results reveal a novel strategy with immense practical potential pertaining to high-contrast X-ray detection.

KEYWORDS

$CsPbBr_3$-DMSO, inorganic perovskites wafer, grain growth, crystal defect, X-ray detector

1 Introduction

X-ray detection is required by medical diagnosis, industrial non-destructive inspection, nuclear reaction monitoring, and other fields [1–3]. There are indirect and direct techniques to detect X-ray. In the indirect mode, X-ray photons are converted to visible light by scintillators and the light is detected by a photodetector. Unfortunately, indirect X-ray imaging suffers from the low spatial resolution and quantum efficiency due to inevitable visible light scattering [4]. In contrast, direct X-ray detectors made of semiconductors absorb X-ray absorption directly and convert X-ray into electrical signals, thus boasting higher sensitivity and spatial imaging resolution [5]. The common direct X-ray conversion semiconductors are silicon (Si), amorphous selenium (a-Se), and Cd(Zn)Te. Nevertheless, Si and a-Se suffer from insufficient X-ray absorption due to the small atomic number and a-Se has lower mobility-lifetime (μτ) products (μτ of 10^{-7} $cm^2 \cdot V^{-1}$) [6]. Cd(Zn)Te is a standard material for hard X-ray detectors but the disadvantages are the high cost and small crystal size [7]. Therefore, it is important to identify semiconducting materials for more efficient direct X-ray detection.

Inorganic metal halide perovskites have emerged to be viable materials for high-contrast X-ray detection due to the large X-ray attenuation coefficient, high carrier mobility, long carrier lifetime, low trap density, and excellent material stability [8–13]. Perovskite single crystals can be prepared in solutions with sufficient thickness and high carrier mobility-lifetime [14, 15]. $CsPbBr_3$ single crystals were first used in X-ray detection in 2013 [16]. Lin et al. have demonstrated the potential of solution-grown $CsPbBr_3$ single crystals for X-ray imaging [17]. After that, Hao and co-workers have reported $CsPbBr_3$ X-ray detectors with a sensitivity of 6021.99 $\mu C \cdot Gy_{air}^{-1} \cdot cm^{-2}$ and detection limit of 1.89 $\mu Gy_{air} \cdot s^{-1}$ [18]. In X-ray imaging, a detector with comparable size to the object being analyzed is necessary because the X-ray refractive index is about 1.0. However, preparation of perovskite single crystals with a large size is challenging and time consuming [19]. In order to absorb high-power X-ray, the thickness of the perovskite film should be hundreds of micrometers, but common solution-based methods such as spin coating and blade coating are commonly employed to produce perovskite films with nanometer-scale thickness designed for solar cells and light-emitting devices [20, 21]. In fact, it is difficult to prepare thick perovskite films due to the low concentration of inorganic perovskite precursors in solutions besides low materials utilization.

Address correspondence to Yanliang Liu, yl.liu4@siat.ac.cn; Xue-Feng Yu, xf.yu@siat.ac.cn

In order to construct a perovskite X-ray converter with a scalable size and the required thickness, an isostatic process has been proposed to compact the perovskite powder to form a polycrystalline perovskite wafer instead of single crystal for X-ray detection and imaging [22]. Tang et al. have developed X-ray detectors consisting of the $Cs_2AgBiBr_6$ wafer with a high sensitivity of 250 $\mu C \cdot Gy_{air}^{-1} \cdot cm^{-2}$ and low signal drifts [23]. Heiss et al. have used $Cs_3Bi_2Br_3I_6$ to fabricate self-healing X-ray detectors with good sustainability and low detection limit [24]. However, the perovskite powder prepared by conventional dry mechanical grinding usually has poor surface morphology and high defect density [25, 26]. Furthermore, solvent-based synthesis of perovskite powders is difficult on a large scale due to the low solubility of the perovskite precursors [27]. Polycrystalline inorganic perovskite wafers normally contain voids and grain boundaries, which decrease the X-ray absorption efficiency and hinder charge transport and collection [23]. In this respect, a high temperature is usually employed to enhance the crystallinity of inorganic perovskite wafers. However, the high temperature inevitably introduces crystal defects, which also renders the integration of perovskite wafers into X-ray imaging flat panels difficult [28, 29].

Herein, a solvent-based approach is designed and demonstrated to produce $CsPbBr_3$ micro-bricks for compact microcrystalline perovskite wafers for X-ray detectors. The $CsPbBr_3$ powder is prepared by mechanical grinding and then cultivated in dimethyl sulfoxide (DMSO) to produce $CsPbBr_3$ micro-bricks with a cubic shape, high crystallinity, and excellent optoelectronic properties. A trace amount of DMSO attaches to the surface of $CsPbBr_3$ micro-bricks via Pb–O bonding, forming the $CsPbBr_3$-DMSO adduct. During hot isostatic processing, the DMSO vapor released from the adduct further promotes $CsPbBr_3$ grain growth, which subsequently merges $CsPbBr_3$ micro-bricks at a low temperature of 100 °C to obtain compact and dense $CsPbBr_3$ wafer with minimized grain boundaries. The wafer exhibits excellent electrical properties such as reduced resistance of 3.16×10^8 Ω·cm and high mobility-lifetime product of 5.16×10^{-4} $cm^2 \cdot V^{-1}$, which are comparable to those of the $CsPbBr_3$ single crystal. The direct X-ray detector with the structure of Au/perovskite/[6,6]-phenyl C61 butyric acid methyl (PCBM)/Au shows a high sensitivity of 14,430 $\mu C \cdot Gy_{air}^{-1} \cdot cm^{-2}$ and low detection limit of 564 $nGy_{air} \cdot s^{-1}$. The detector also has excellent stability at an electric field of 40 $V \cdot mm^{-1}$ and dose rate of 1620 $\mu Gy_{air} \cdot s^{-1}$.

2 Materials and methods

2.1 Chemicals

$PbBr_2$ (lead bromide, 99%, Aladdin), CsBr (cesium bromide, 99.5%, Aladdin), and organic solvents such as dimethyl sulfoxide (DMSO, AR, 99%), acetone (AR, 99%), and isopropyl (AR, 99%) were supplied from Sigma-Aldrich. PCBM (AR, 99%) was provided by Xi'an Polymer Light Corp. The gold particles (product No. Au11474 3 × 3 mm) used to prepare the gold electrode were purchased from Zhong Nuo New Materials Co., Ltd. (Beijing, China). All the chemicals were used as received without further purification.

2.2 Synthesis of $CsPbBr_3$ micro-bricks

The pristine $CsPbBr_3$ powder was synthesized by mechanical milling. The reactants (17.36 g, CsBr/$PbBr_2$ = 1/1) were milled with 40 g agate balls for 2 h at 400 rpm in a planetary ball mill machine. In the following, the pristine $CsPbBr_3$ powder was cultivated in DMSO (1 mL per 1 g of powder) under stirring at room temperature, and then extracted from isopropanol. After drying at 40 °C for overnight, $CsPbBr_3$ micro-bricks were obtained.

2.3 Preparation of $CsPbBr_3$ wafer

The pristine $CsPbBr_3$ and $CsPbBr_3$ micro-bricks powders were squashed onto the perovskite wafer with mirror-like surface, respectively. Subsequently, the perovskite wafers were further heated at 150 °C for 2 h to evaporate the residual DMSO, obtaining complete $CsPbBr_3$ wafers.

2.4 Device fabrication

The X-ray detector has device configuration of Au (80 nm)/PCBM/$CsPbBr_3$ wafer/Au (80 nm). The PCBM solution (20 $mg \cdot mL^{-1}$) layer was spin-coated on the free-standing perovskite wafer at 1500 rpm for 30 s. The Au film was deposited onto both sides of the $CsPbBr_3$/PCBM wafer by thermal evaporation. The X-ray detector has an effective device area of 0.01 cm^2 (1 mm × 1 mm), defined by the overlapping area of the top and bottom Au electrodes.

3 Results and discussion

In X-ray detectors, a thick perovskite film is required to absorb high energy X-ray. Herein, preparation of the high-quality raw $CsPbBr_3$ powder is illustrated in Fig. 1(a). A large amount of $CsPbBr_3$ powder is first synthesized by simple mechanical grinding (Fig. S1 in the Electronic Supplementary Material (ESM)). However, the as-prepared $CsPbBr_3$ powder has an irregular morphology with a wide grain size distribution ranging from several nanometers to micrometers (Fig. S2 in the ESM), and so DMSO is introduced to modify the $CsPbBr_3$ powder. As shown in Fig. S3 in the ESM, the $CsPbBr_3$ powder is immersed in DMSO and stirred to mix completely. After aging for 2 h, the yellow $CsPbBr_3$ mixture converts to yellowish green and isopropanol is added as an anti-solvent to precipitate $CsPbBr_3$. In the synthesis, the $CsPbBr_3$ powder dissolves and regrows to form cubic $CsPbBr_3$ micro-bricks with a large size of several micrometers, as shown in Fig. 1(b) and Fig. S4 in the ESM.

To monitor the structural changes, X-ray diffraction (XRD) is conducted as shown in Fig. 1(c). The diffraction patterns of the pristine $CsPbBr_3$ powder and $CsPbBr_3$ micro-bricks can be well indexed to the standard monoclinic perovskite phase of $CsPbBr_3$ (PDF#18-0364). In particular, the stronger XRD peaks of $CsPbBr_3$ micro-bricks indicate the improved crystallinity compared with the pristine $CsPbBr_3$. Besides, the pristine $CsPbBr_3$ powder shows the strongest diffraction peak at 2θ = 21.50°, which is corresponding to the (110) facet of the monoclinic $CsPbBr_3$ phase. In contrast, the $CsPbBr_3$ micro-bricks exhibit two impressive diffraction peaks at 2θ = 15.21° and 30.70° assigned to the (100) and (200) facets of the monoclinic $CsPbBr_3$ phase, respectively, which demonstrates the <100> preferred orientation selectively [30–31]. The pattern of the yellowish green precipitate can be indexed to Cs_4PbBr_6 (PDF#54-0750) with the prominent peaks of (024). The formation of intermediate Cs_4PbBr_6 can be explained by the solubility difference between $PbBr_2$ and CsBr. Based on the above observations, it is assumed that the synthesis of $CsPbBr_3$ micro-bricks can be divided into three stages: dissolution, recrystallization, and precipitation. As illustrated in Fig. S5 in the ESM, in the first stage, the pristine perovskite powder dissolves partially in DMSO. Since Pb^{2+} is more soluble in this condition than Cs^+, Cs_4PbBr_6 is formed with Cs-rich <012> preferred orientation [32]. After aging for a while, dynamic equilibrium in the DMSO solution is achieved, and Cs_4PbBr_6 recrystallizes to the appearance of micrometer-scale flakes gradually, as shown in Fig. S6 in the ESM [32, 33]. With the addition of anti-solvent, the

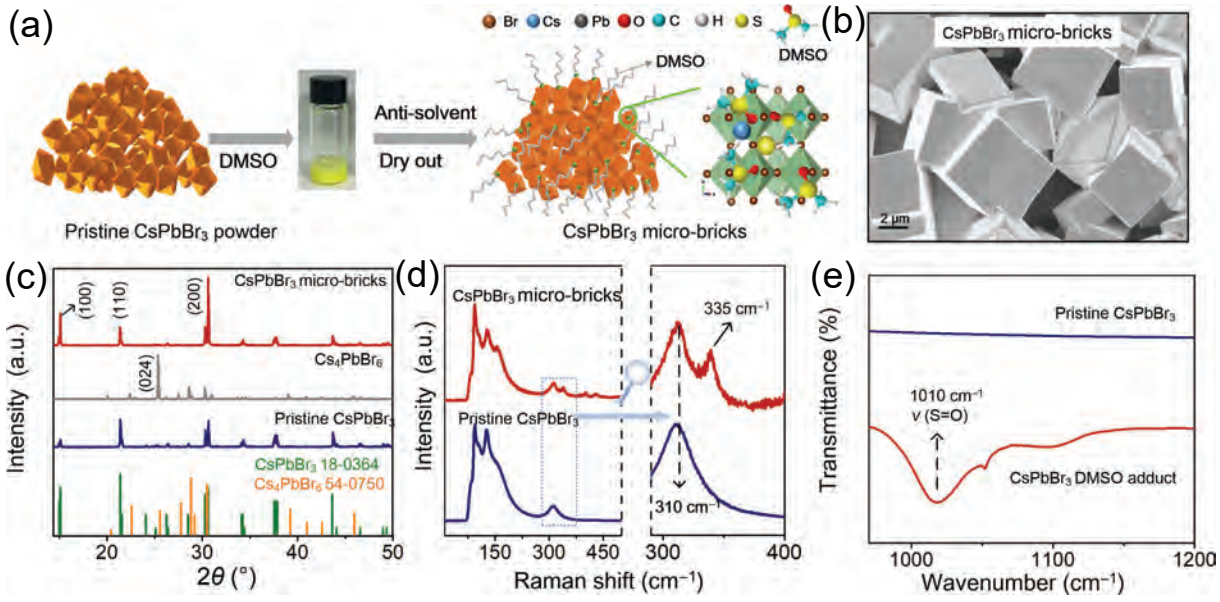

Figure 1 Synthesis and characterization of $CsPbBr_3$ micro-bricks and $CsPbBr_3$ DMSO adduct. (a) Schematic illustration of the preparation of the $CsPbBr_3$ micro-bricks powder. (b) SEM image of the $CsPbBr_3$ micro-bricks. (c) XRD patterns of the pristine $CsPbBr_3$, Cs_4PbBr_6, and $CsPbBr_3$ micro-bricks. (d) Raman scattering spectra and (e) FTIR spectra of the pristine $CsPbBr_3$ and $CsPbBr_3$ DMSO adduct (inset showing the Tauc plot).

dissolved $PbBr_2$ and CsBr undergo rapid crystallization and precipitate from the solution. Owing to the lower atom density and energy, $CsPbBr_3$ grows along the <100> orientation and finally the micro-bricks are obtained [30]. It is worth noting that, the aging time and the type of the anti-solvents play an important role in determining the formation of the $CsPbBr_3$ micro-bricks (Figs. S7 and S8 in the ESM). Moreover, the $CsPbBr_3$ powder is exposed to 85 °C and 85% relative humidity condition to evaluate the stability. After 21 days of aging under high temperature and humidity, compared with the pristine $CsPbBr_3$ transformed to $CsPb_2Br_5$ phase (PDF#25-0211), the $CsPbBr_3$ micro-bricks exhibit significantly improved tolerance to moisture and temperature with stable $CsPbBr_3$ cubic perovskite phase (Fig. S9 in the ESM).

The Raman scattering spectra are presented in Fig. 1(d). According to previous reports, the second order Raman band at 310 cm^{-1} observed from all the samples indicates the presence of $CsPbBr_3$ [34] and the Raman peaks below 200 cm^{-1} are similar. The peak at 335 cm^{-1} reveals that a small amount of DMSO remains in $CsPbBr_3$ micro-bricks [35]. To further investigate the structure, the Fourier-transform infrared (FTIR) results are displayed in Fig. 1(e). In contrast to the pristine $CsPbBr_3$, the $CsPbBr_3$ micro-bricks exhibits an additional peak at 1011 cm^{-1} ascribed to stretching of S=O in DMSO. Generally, the FTIR peak of S=O of DMSO is at 1048 cm^{-1} and the decrease in the vibration frequencies from 1048 to 1011 cm^{-1} is related to weaker bonding strength of S=O, indicating coordination between $CsPbBr_3$ and DMSO [36, 37]. The X-ray photoelectron spectroscopy (XPS) is further conducted to investigate the formation mechanism of $CsPbBr_3$-DMSO adducts. As shown in Fig. S10 in the ESM, the peaks at 137.9 and 142.8 eV are attributed to Pb $4f_{7/2}$ and $4f_{5/2}$, respectively (Fig. 1(c)). Compared with the pristine $CsPbBr_3$, the Pb 4f of adduct presents an obvious shift to higher binding energy and two shoulders (~ 139.5 and ~ 144.2 eV), suggesting the existence of Pb–O coordination [38, 39]. It has been shown that formation of intermediate adducts between the lead halide perovskite and DMSO proceeds via the Pb–O bridge [40, 41]. Hence, it can be postulated that the $CsPbBr_3$ micro-bricks powder contains some $CsPbBr_3$-DMSO adducts. Moreover, as shown in Fig. S11 in the ESM, the disappearance of the S=O peaks after 100 °C heating indicates that $CsPbBr_3$-DMSO complex can be easily broken down to $CsPbBr_3$ and DMSO vapor. The released DMSO vapor is expected to enhance the growth of the $CsPbBr_3$ crystal.

As shown in Fig. 2, the pristine $CsPbBr_3$ and $CsPbBr_3$ micro-bricks are squashed into perovskite wafers by hot isostatic pressing at 100 °C and 10 MPa for 1 h. The samples were further heated at 150 °C for 2 h on a hot plate to form the $CsPbBr_3$ wafers. The thickness of perovskite wafer varies with the amount of powder added, ranging from 300 to 600 μm (Fig. S12 in the ESM). Scanning electron microscopy (SEM) and atom force microscopy (AFM) are conducted to examine the morphology of the two samples. The $CsPbBr_3$ wafer exhibits an incomplete and non-uniform surface morphology with a small grain size and lots of pinholes as shown in Fig. 2(b), and the interior shows many voids and grain boundaries as shown in Fig. 2(c), which are detrimental to X-ray absorption as well as charge transport and collection. The same surface morphology can be observed by AFM image as shown in Fig. 2(d). In contrast, the wafer made of $CsPbBr_3$ micro-bricks exhibits compact surface with a large grain size and full coverage, as well dense interior with little voids and merged grain boundaries as shown in Figs. 2(e) and 2(f). The improved morphology can be attributed to the *in situ* growth of $CsPbBr_3$ induced by DMSO vapor during hot isostatic processing. The AFM image in Fig. 2(g) corroborates grain growth and merged grain boundaries, and the pristine and $CsPbBr_3$ micro-bricks wafers exhibit comparable surface roughness of 46.1 and 28.5 nm in Fig. S13 in the ESM, respectively. Therefore, it is reasonable to speculate that DMSO plays a vital role in the growth of the $CsPbBr_3$ micro-bricks. The influence of humidity on the wafer is also investigated. After 14 days in air (25 °C and 60% relative humidity), the $CsPbBr_3$ micro-bricks wafer still maintains good morphology, while the pristine $CsPbBr_3$ wafer exhibits obvious decomposition along grain boundaries (Fig. S14 in the ESM).

The steady-state photoluminescence (PL) and time-resolved photoluminescence (TRPL) characteristics are analyzed to determine the optical properties, as shown in Figs. 3(a) and 3(b). The wafer made of $CsPbBr_3$ micro-bricks exhibits significantly higher PL intensity than the $CsPbBr_3$ wafer and the PL peak red-shifts from 515 to 518 nm indicative of a larger grain size and enhanced crystallinity. The diffuse reflectance data are presented in Fig. S15 in the ESM and the optical absorption is analyzed by Kubelka–Munk equation. In the wavelength range of 500–550 nm, the reflectance of the pristine $CsPbBr_3$ is slightly higher than that of the $CsPbBr_3$ micro-bricks powder caused by light scattering

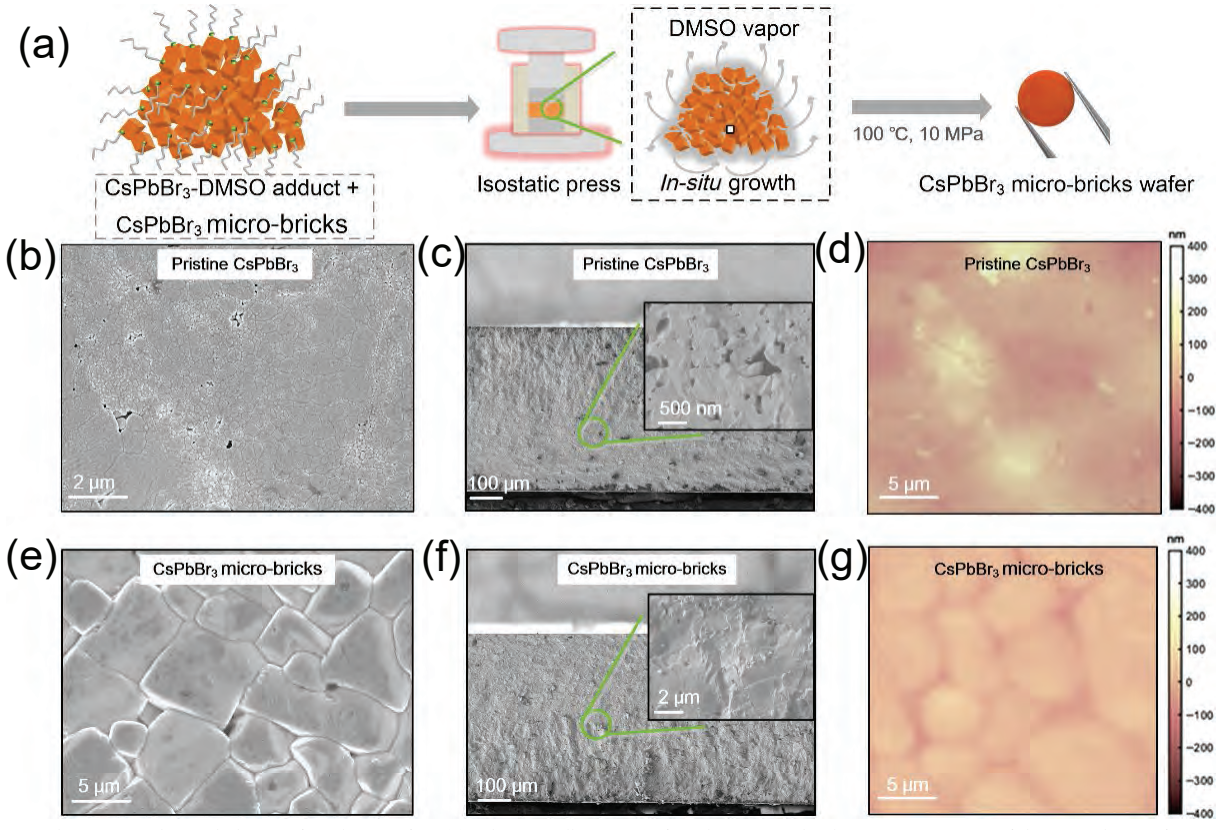

Figure 2 Fabrication and morphologies of $CsPbBr_3$ wafers. (a) Schematic illustration of $CsPbBr_3$ micro-bricks isostatic pressing of the perovskite wafer. SEM and AFM images of ((b), (c), and (d)) pristine $CsPbBr_3$ and ((e), (f), and (g)) $CsPbBr_3$ micro-bricks perovskite wafer.

at grain boundaries. By fitting the spectra with the Tauc relationship, the bandgap E_g values of the pristine $CsPbBr_3$ and $CsPbBr_3$ micro-bricks are calculated to be 2.27 and 2.25 eV, respectively. The narrower bandgap can be attributed to the larger grain size [42]. The TRPL of the untreated $CsPbBr_3$ and $CsPbBr_3$ micro-bricks wafers can be fitted by exponential functions, where A_1 and A_2 are the fractional contributions of the PL decay lifetime. A short lifetime (τ_1) corresponds to fast decay related to quenching (including charge transfer) and defects, whereas a long lifetime (τ_2) corresponds to slow decay due to recombination. The pristine $CsPbBr_3$ wafer shows a short lifetime τ_1 of 2.29 ns and long lifetime τ_2 of 11.74 ns. In comparison, the $CsPbBr_3$ micro-bricks wafer exhibits an obviously longer short lifetime τ_1 of 5.70 ns and long lifetime τ_2 of 33.07 ns. τ_{ave} improves from 6.80 to 25.92 ns, suggesting a smaller defect density and enhanced carrier transport in the $CsPbBr_3$ micro-bricks wafer. The TRPL parameters are listed in Table S1 in the ESM. The $CsPbBr_3$ micro-bricks wafer also has higher crystallinity than the pristine $CsPbBr_3$ wafer as shown in Fig. 3(c) [43], which is consistent with Fig. 1(d). All in all, the $CsPbBr_3$ micro-bricks wafer has better crystallinity and lower defect density boding well for charge transport and collection.

To determine the optoelectronic properties, photoconductivity measurements are carried out as shown in Fig. 3(g). The photocurrent response is monitored by applying voltages from 0 to 50 V as shown in Fig. 3(g). The Hecht formula is employed to fit the photocurrent–voltage curve (Eq. (1))

$$I = I_0 \mu\tau V/L^2(1-\exp(-L^2/\mu\tau V)) \quad (1)$$

where I_0 is the saturated current, L is the $CsPbBr_3$ wafer thickness, and V is the applied voltage. The μτ products of the pristine $CsPbBr_3$ and $CsPbBr_3$ micro-bricks wafers are determined to be 1.66×10^{-5} and 5.16×10^{-4} $cm^2 \cdot V^{-1}$, respectively, and a bigger μτ product normally indicates higher crystallinity and lower defect density. The ion migration of perovskite wafer was further investigated through Kelvin probe force microscopy (KPFM) measurement (Fig. S16 in the ESM), and the $CsPbBr_3$ micro-bricks wafer exhibits significantly lower electric potential than the pristine $CsPbBr_3$ wafer. The ions have lower formation energy and diffusion barriers compared to other mobile species in $CsPbBr_3$ wafer, which easily migrates under an applied electric field, leading to high electric potential. Therefore, the lower electric potential indicates reduced suppressed ion migration in the $CsPbBr_3$ micro-bricks wafer. As shown in Fig. 3(e), the pristine $CsPbBr_3$ wafer has a higher resistivity of 2.2×10^9 Ω·cm than that of $CsPbBr_3$ micro-bricks wafer, on account of the interior voids and holes decrease electrical conductivity, which is consistent with the SEM results.

Based on ultraviolet photoelectron spectra (UPS) results, the work function (WF) and valance band maximum (VBM) of $CsPbBr_3$ are calculated to be −4.51 and −5.80 eV, respectively. Combined with ultraviolet–visible (UV–Vis) spectroscopy, energy level alignment of the X-ray detector (Au/$CsPbBr_3$/PCBM/Au) is illustrated in Fig. S17 in the ESM. Figure 3(f) shows the current density–voltage (J–V) characteristics of the X-ray detectors constructed with the pristine $CsPbBr_3$ and $CsPbBr_3$ micro-bricks wafers. The $CsPbBr_3$ micro-bricks detector shows obviously higher light currents and response, confirming better X-ray detection. The dark current density of the $CsPbBr_3$ micro-brick detector (3.04 μA·cm^{-2}) is a little higher than that of 0. 896 μA·cm^{-2} observed from the other detector at an electric field of 100 V·mm^{-1}, which is consistent of the resistivity. However, the light current of the $CsPbBr_3$ micro-bricks detector (21.8 μA·cm^{-2}) is ten times higher than that of the detector constructed with the pristine materials (2.4 μA·cm^{-2}), thus facilitating low-dose and high-sensitivity X-ray detection.

To obtain more dynamic information, the time-resolved current densities of the pristine $CsPbBr_3$ and $CsPbBr_3$ micro-bricks detectors for X-ray dose rates from 1620 to 160 μGy_{air}·s^{-1} are presented in Fig. 4(a). Both detectors show decent response signals

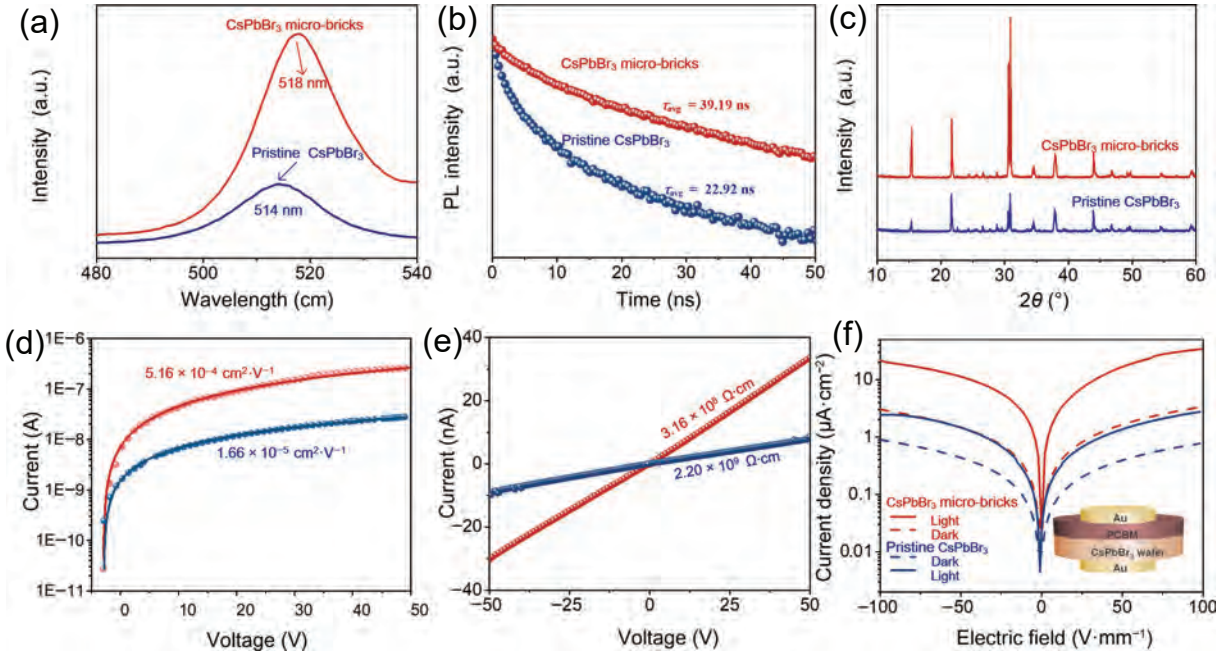

Figure 3 Optoelectronic properties of $CsPbBr_3$ wafer. (a) PL spectra, (b) TRPL spectra, (c) XRD patterns, (d) photoconductivity, and (e) resistivity of the pristine $CsPbBr_3$ and $CsPbBr_3$ micro-bricks wafer. (f) *J*–*V* characteristics of the pristine $CsPbBr_3$ and $CsPbBr_3$ micro-bricks detectors.

upon on/off X-ray switching. In general, the $CsPbBr_3$ micro-bricks detector shows a lower dark current density and larger X-ray on-off ratio than conventional detectors. To quantify the sensitivity of the two detectors, the X-ray generated current densities are plotted as a function of dose rates in Figs. 4(b) and 4(c). A linear relationship is observed between 1620 and 160 $\mu Gy_{air} \cdot s^{-1}$. The sensitivity can be calculated from the slope of the photocurrents versus X-ray dose rates plots acquired at different electric fields. The pristine $CsPbBr_3$ detector exhibits X-ray sensitivities of 798, 675, 521, and 252 $\mu C \cdot Gy_{air}^{-1} \cdot cm^{-2}$ at 100, 80, 60, and 40 $V \cdot mm^{-1}$, respectively. In comparison, the $CsPbBr_3$ micro-bricks detector shows much higher sensitivity of 14,430, 9810, 5170, and 2640 $\mu C \cdot Gy_{air}^{-1} \cdot cm^{-2}$ at electric fields of 100, 80, 60, and 40 $V \cdot mm^{-1}$, respectively.

To further assess the performance, the signal-to-noise ratio (SNR) based on the noise calculated from the standard deviation of the photocurrents is derived by the following Eq. (2)

$$\mathrm{SNR} = I_{\mathrm{signal}}/I_{\mathrm{noise}} = (I_{\mathrm{photo}} - I_{\mathrm{dark}})/I_{\mathrm{noise}} \quad (2)$$

where I_{signal} is the signal current, I_{noise} is the noise current, I_{photo} is the average current under X-ray irradiation, and I_{dark} is the average dark current derived from parallel experiments conducted at each bias. The SNRs of the detectors as a function of dose rates are plotted in Fig. 4(d). A large electric field of 100 $V \cdot mm^{-1}$ is applied

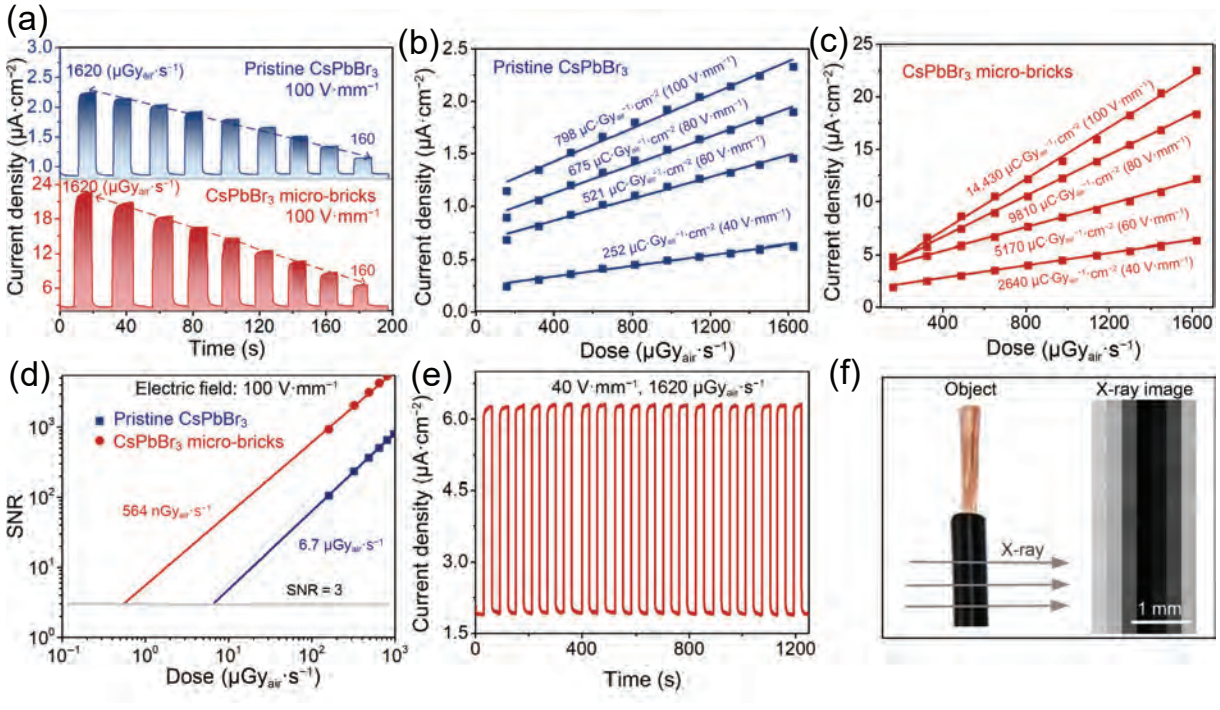

Figure 4 X-ray detection performance based on $CsPbBr_3$ wafer devices. (a) X-ray response profiles of the pristine $CsPbBr_3$ and $CsPbBr_3$ micro-bricks X-ray detectors. X-ray generated current densities as a function of dose rates at different applied electrical fields: (b) Pristine $CsPbBr_3$ and (c) $CsPbBr_3$ micro-bricks X-ray detector. (d) Dose rate dependent SNR of the detectors. (e) Stability of the pristine $CsPbBr_3$ detector under pulsed X-ray irradiation of 1620 $\mu Gy_{air} \cdot s^{-1}$. (f) Optical image and X-ray image of an electrical wire.

to the opposite electrodes to extract X-ray generated charges in the interior of the thick $CsPbBr_3$ wafer. The SNR exhibits a linear dependence with X-ray dose rates. According to the International Union of Pure and Applied Chemistry standard, the detector signal should maintain an SNR of over 3. As expected, the $CsPbBr_3$ micro-bricks detector shows a low limit-of-detection (LoD) of 564 $nGy_{air}·s^{-1}$ in contrast to 6.75 $\mu Gy_{air}·s^{-1}$ for the conventional detector.

To evaluate the stability under normal operating conditions, X-ray on/off experiments are carried out for 30 s at a 40 $V·mm^{-1}$ external electric field and 1620 $\mu Gy_{air}·s^{-1}$ X-ray dose and the results are presented in Fig. 4(e) and Fig. S18 in the ESM. Compared to the $CsPbBr_3$ detector, the $CsPbBr_3$ micro-bricks detector exhibits a more reproducible and stable response with small changes. Moreover, the device is placed in the ambient condition for a period of time to test the storage stability. After 14 days in air (25 °C, relative humidity 60%), the pristine $CsPbBr_3$ detector exhibits enhanced dark current but reduced photocurrent response, in contrast, the $CsPbBr_3$ micro-bricks detector maintains satisfactory device performance (Fig. S19 in the ESM). The X-ray imaging capability is assessed by *x*–*y* scanning experiments, in which an electric wire is the imaging target. As shown in Fig. 4(f), the capability is confirmed.

4 Conclusions

A DMSO-based solution process is demonstrated to produce high-quality $CsPbBr_3$ micro-bricks for dense and compact microcrystalline perovskite wafers for X-ray detection. A large amount of $CsPbBr_3$ powder can be prepared by mechanical grinding. The $CsPbBr_3$ micro-bricks powder with a cubic shape, high crystallinity, and excellent optical properties is prepared. A trace amount of DMSO attaches to the $CsPbBr_3$ micro-bricks via Pb–O bonding to form the $CsPbBr_3$-DMSO adduct. During hot isostatic processing, the DMSO vapor released from $CsPbBr_3$-DMSO promotes $CsPbBr_3$ grain growth and merges $CsPbBr_3$ micro-bricks, resulting in a compact and dense wafer with a large grain size and minimized grain boundaries. The $CsPbBr_3$ micro-bricks wafer has excellent optoelectronic properties as exemplified by a large μτ product of 5.16×10^{-4} $cm^2·V^{-1}$, and the X-ray detector exhibits high sensitivity of 14,430 $\mu C·Gy_{air}^{-1}·cm^{-2}$, low detection limit of 564 $nGy_{air}·s^{-1}$, as well as robust stability. The results reveal an efficient strategy to design and produce sensitive and sturdy X-ray detectors.

Acknowledgements

This work was financially supported by the National Natural Science Foundation of China (Nos. 21975280, 62004091, and 12235006), the Shenzhen Excellent Science and Technology Innovation Talent Training Project - Outstanding Youth Project (No. RCJC20200714114435061), the Shenzhen Basic Research Program (No. JCYJ20200109115212546), the Chinese Academy of Sciences Special Research Assistant Project (Nos. Y95909 and E15907), the Chinese Academy of Sciences Excellent Youth Innovation Fund grade B (No. E2G0161001), the Youth Innovation Promotion Association Chinese Academy of Sciences (No. 2020354), the Hong Kong ITC (Innovation and Technology Commission) ITF (Innovation and Technology Fund) (Nos. GHP/149/20SZ and CityU 9440296), and the City University of Hong Kong Donation Research Grant (DON-RMG No. 9229021).

Electronic Supplementary Material: Supplementary material (further details of the characterization, SEM images, AFM images, KPFM images, schematic illustration, XRD patterns, XPS spectra, FTIR spectra, UPS spectra, and stability tests) is available in the online version of this article at https://doi.org/10.1007/s12274-023-5487-3.

References

[1] Ozturk, T.; Talo, M.; Yildirim, E. A.; Baloglu, U. B.; Yildirim, O.; Acharya, U. R. Automated detection of COVID-19 cases using deep neural networks with X-ray images. *Comput. Biol. Med.* **2020**, *121*, 103792.

[2] Sakdinawat, A.; Attwood, D. Nanoscale X-ray imaging. *Nat. Photonics* **2010**, *4*, 840–848.

[3] Casalta, S.; Daquino, G. G.; Metten, L.; Oudaert, J.; Van De Sande, A. Digital image analysis of X-ray and neutron radiography for the inspection and the monitoring of nuclear materials. *NDT & E Int.* **2003**, *36*, 349–355.

[4] Zhou, F. G.; Li, Z. Z.; Lan, W.; Wang, Q.; Ding, L. M.; Jin, Z. W. Halide perovskite, a potential scintillator for X-ray detection. *Small Methods* **2020**, *4*, 2000506.

[5] Li, Z. Z.; Zhou, F. G.; Yao, H. H.; Ci, Z.; Yang, Z.; Jin, Z. W. Halide perovskites for high-performance X-ray detector. *Mater. Today* **2021**, *48*, 155–175.

[6] Kasap, S. O. X-ray sensitivity of photoconductors: Application to stabilized a-Se. *J. Phys. D Appl. Phys.* **2000**, *33*, 2853–2865.

[7] Street, R. A.; Ready, S. E.; Lemmi, F.; Shah, K. S.; Bennett, P.; Dmitriyev, Y. Electronic transport in polycrystalline PbI_2 films. *J. Appl. Phys.* **1999**, *86*, 2660–2667.

[8] Liang, J.; Wang, C. X.; Wang, Y. R.; Xu, Z. R.; Lu, Z. P.; Ma, Y.; Zhu, H. F.; Hu, Y.; Xiao, C. C.; Yi, X. et al. All-inorganic perovskite solar cells. *J. Am. Chem. Soc.* **2016**, *138*, 15829–15832.

[9] Liu, C.; Li, W. Z.; Zhang, C. L.; Ma, Y. P.; Fan, J. D.; Mai, Y. All-inorganic $CsPbI_2Br$ perovskite solar cells with high efficiency exceeding 13%. *J. Am. Chem. Soc.* **2018**, *140*, 3825–3828.

[10] Leguy, A. M. A.; Frost, J. M.; McMahon, A. P.; Sakai, V. G.; Kockelmann, W.; Law, C.; Li, X. E.; Foglia, F.; Walsh, A.; O' Regan, B. C. et al. The dynamics of methylammonium ions in hybrid organic–inorganic perovskite solar cells. *Nat. Commun.* **2015**, *6*, 7124.

[11] Zhang, L. Q.; Yang, X. L.; Jiang, Q.; Wang, P. Y.; Yin, Z. G.; Zhang, X. W.; Tan, H. R.; Yang, Y.; Wei, M. Y.; Sutherland, B. R. et al. Ultra-bright and highly efficient inorganic based perovskite light-emitting diodes. *Nat. Commun.* **2017**, *8*, 15640.

[12] Wang, C.; Xiao, J. W.; Yan, Z. G.; Niu, X. W.; Lin, T. F.; Zhou, Y. C.; Li, J. Y.; Han, X. D. Colloidal synthesis and phase transformation of all-inorganic bismuth halide perovskite nanoplates. *Nano Res.* **2023**, *16*, 1703–1711.

[13] Dierks, H.; Zhang, Z. J.; Lamers, N.; Wallentin, J. 3D X-ray microscopy with a $CsPbBr_3$ nanowire scintillator. *Nano Res.* **2023**, *16*, 1084–1089.

[14] Zhang, H. J.; Wang, F. B.; Lu, Y. F.; Sun, Q. H.; Xu, Y. D.; Zhang, B. B.; Jie, W.; Kanatzidis, M. G. High-sensitivity X-ray detectors based on solution-grown caesium lead bromide single crystals. *J. Mater. Chem. C* **2020**, *8*, 1248–1256.

[15] Li, W. J.; Li, H. Y.; Song, J. M.; Guo, C. J.; Zhang, H. M.; Wei, H. T.; Yang, B. Fine-control-valve of halide perovskite single crystal quality for high performance X-ray detection. *Sci. Bull.* **2021**, *66*, 2199–2206.

[16] Stoumpos, C. C.; Malliakas, C. D.; Peters, J. A.; Liu, Z. F.; Sebastian, M.; Im, J.; Chasapis, T. C.; Wibowo, A. C.; Chung, D. Y.; Freeman, A. J. et al. Crystal growth of the perovskite semiconductor $CsPbBr_3$: A new material for high-energy radiation detection. *Cryst. Growth Des.* **2013**, *13*, 2722–2727.

[17] Peng, J. L.; Xia, C. Q.; Xu, Y. L.; Li, R. M.; Cui, L. H.; Clegg, J. K.; Herz, L. M.; Johnston, M. B.; Lin, Q. Q. Crystallization of $CsPbBr_3$ single crystals in water for X-ray detection. *Nat. Commun.* **2021**, *12*, 1531.

[18] Di, J. Y.; Li, H. J.; Su, J.; Yuan, H. D.; Lin, Z. H.; Zhao, K.; Chang, J. J.; Hao, Y. Reveal the humidity effect on the phase pure $CsPbBr_3$ single crystals formation at room temperature and its application for

ultrahigh sensitive X-ray detector. *Adv. Sci.* **2022**, *9*, 2103482.
[19] Ding, J. X.; Du, S. J.; Zuo, Z. Y.; Zhao, Y.; Cui, H. Z.; Zhan, X. Y. High detectivity and rapid response in perovskite $CsPbBr_3$ single-crystal photodetector. *J. Phys. Chem. C* **2017**, *121*, 4917–4923.
[20] Pan, W. C.; Yang, B.; Niu, G. D.; Xue, K. H.; Du, X. Y.; Yin, L. X.; Zhang, M. Y.; Wu, H. D.; Miao, X. S.; Tang, J. Hot-pressed $CsPbBr_3$ quasi-monocrystalline film for sensitive direct X-ray detection. *Adv. Mater.* **2019**, *31*, 1904405.
[21] Wang, X.; Shi, H. F.; Ma, H. L.; Ye, W. P.; Song, L. L.; Zan, J.; Yao, X. K.; Ou, X. Y.; Yang, G. H.; Zhao, Z. et al. Organic phosphors with bright triplet excitons for efficient X-ray-excited luminescence. *Nat. Photonics* **2021**, *15*, 187–192.
[22] Shrestha, S.; Fischer, R.; Matt, G. J.; Feldner, P.; Michel, T.; Osvet, A.; Levchuk, I.; Merle, B.; Golkar, S.; Chen, H. W. et al. High-performance direct conversion X-ray detectors based on sintered hybrid lead triiodide perovskite wafers. *Nat. Photonics* **2017**, *11*, 436–440.
[23] Yang, B.; Pan, W. C.; Wu, H. D.; Niu, G. D.; Yuan, J. H.; Xue, K. H.; Yin, L. X.; Du, X. Y.; Miao, X. S.; Yang, X. Q. et al. Heteroepitaxial passivation of $Cs_2AgBiBr_6$ wafers with suppressed ionic migration for X-ray imaging. *Nat. Commun.* **2019**, *10*, 1989.
[24] Daum, M.; Deumel, S.; Sytnyk, M.; Afify, H. A.; Hock, R.; Eigen, A.; Zhao, B. L.; Halik, M.; These, A.; Matt, G. J. et al. Self-healing $Cs_3Bi_2Br_3I_6$ perovskite wafers for X-ray detection. *Adv. Funct. Mater.* **2021**, *31*, 2102713.
[25] López, C. A.; Abia, C.; Alvarez-Galván, M. C.; Hong, B. K.; Martínez-Huerta, M. V.; Serrano-Sánchez, F.; Carrascoso, F.; Castellanos-Gómez, A.; Fernández-Díaz, M. T.; Alonso, J. A. Crystal structure features of $CsPbBr_3$ perovskite prepared by mechanochemical synthesis. *ACS Omega* **2020**, *5*, 5931–5938.
[26] Palazon, F.; El Ajjouri, Y.; Sebastia-Luna, P.; Lauciello, S.; Manna, L.; Bolink, H. J. Mechanochemical synthesis of inorganic halide perovskites: Evolution of phase-purity, morphology, and photoluminescence. *J. Mater. Chem. C* **2019**, *7*, 11406–11410.
[27] Rakita, Y.; Kedem, N.; Gupta, S.; Sadhanala, A.; Kalchenko, V.; Böhm, M. L.; Kulbak, M.; Friend, R. H.; Cahen, D.; Hodes, G. Low-temperature solution-grown $CsPbBr_3$ single crystals and their characterization. *Cryst. Growth Des.* **2016**, *16*, 5717–5725.
[28] Liu, Y.; Zhu, X. F.; Li, M. R.; Liu, H. Y.; Cong, Y.; Yang. W. S. Stabilization of low-temperature degradation in mixed ionic and electronic conducting perovskite oxygen permeation membranes. *Angew. Chem., Int. Ed.* **2013**, *125*, 3314–3318.
[29] Wei, W.; Zhang, Y.; Xu, Q.; Wei, H. T.; Fang, Y. J.; Wang, Q.; Deng, Y. H.; Li, T.; Gruverman, A.; Cao, L. et al. Monolithic integration of hybrid perovskite single crystals with heterogenous substrate for highly sensitive X-ray imaging. *Nat. Photonics* **2017**, *11*, 315–321.
[30] Dong, S. H.; Hu, Z. Y.; Wei, P.; Han, J. R.; Wang, Z.; Liu, J.; Su, B. L.; Zhao, D. Y.; Liu, Y. All-inorganic perovskite single-crystal photoelectric anisotropy. *Adv. Mater.* **2022**, *34*, 2204342.
[31] Zhang, C. X.; Chen, J. Y.; Wang, S.; Kong, L. M.; Lewis, S. W.; Yang, X. Y.; Rogach, A. L.; Jia, G. H. Metal halide perovskite nanorods: Shape matters. *Adv. Mater.* **2020**, *32*, 2002736.
[32] Zhou, B.; Ding, D.; Wang, Y.; Fang, S. F.; Liu, Z. X.; Tang, J.; Li, H. N.; Zhong, H. Z.; Tian, B. B.; Shi, Y. M. A scalable H_2O-DMF-DMSO solvent synthesis of highly luminescent inorganic perovskite-related cesium lead bromides. *Adv. Opt. Mater.* **2021**, *9*, 2001435.
[33] Lou, S. Q.; Xuan, T. T.; Liang, Q. Y.; Huang, J. J.; Cao, L. Y.; Yu, C. Y.; Cao, M. M.; Xia, C.; Wang, J.; Zhang, D. F. et al. Controllable and facile synthesis of $CsPbBr_3$-Cs_4PbBr_6 perovskite composites in pure polar solvent. *J. Colloid Interface Sci.* **2019**, *537*, 384–388.
[34] Qin, Z. J.; Dai, S. Y.; Hadjiev, V. G.; Wang, C.; Xie, L. X.; Ni, Y. Z.; Wu, C. Z.; Yang, G.; Chen, S.; Deng, L. Z. et al. Revealing the origin of luminescence center in 0D Cs_4PbBr_6 perovskite. *Chem. Mater.* **2019**, *31*, 9098–9104.
[35] Nielsen, O. F.; Christensen, D. H.; Praestgaard, E. Interaction between dimethylsulfoxide and formamide in the liquid state. *J. Chem. Phys.* **1985**, *82*, 1183–1185.
[36] Ahn, N.; Son, D. Y.; Jang, I. H.; Kang, S. M.; Choi, M.; Park, N. G. Highly reproducible perovskite solar cells with average efficiency of 18.3% and best efficiency of 19.7% fabricated via lewis base adduct of lead(II) iodide. *J. Am. Chem. Soc.* **2015**, *137*, 8696–8699.
[37] Gu, E. N.; Tang, X. F.; Langner, S.; Duchstein, P.; Zhao, Y. C.; Levchuk, I.; Kalancha, V.; Stubhan, T.; Hauch, J.; Egelhaaf, H. J. et al. Robot-based high-throughput screening of antisolvents for lead halide perovskites. *Joule* **2020**, *4*, 1806–1822.
[38] Huang, W. X.; Manser, J. S.; Kamat, P. V.; Ptasinska, S. Evolution of chemical composition, morphology, and photovoltaic efficiency of $CH_3NH_3PbI_3$ perovskite under ambient conditions. *Chem. Mater.* **2016**, *28*, 303–311.
[39] Chen, S. H.; Zhong, Q. X.; Liu, J.; Guan, W. H.; Li, P. L.; Mahmood, I.; Cao, M. H.; Zhang, Q. Improved photophysical properties and durability of $CsPbBr_3$ NCs endowed by inorganic oxoacid and bromide ions. *Nanoscale* **2021**, *13*, 9634–9640.
[40] Kim, B. W.; Heo, J. H.; Park, J. K.; Lee, D. S.; Park, H.; Kim, S. Y.; Kim, J. H.; Im, S. H. Morphology controlled nanocrystalline $CsPbBr_3$ thin-film for metal halide perovskite light emitting diodes. *J. Ind. Eng. Chem.* **2021**, *97*, 417–425.
[41] Wang, H. R.; Zhang, X. Y.; Wu, Q. Q.; Cao, F.; Yang, D. W.; Shang, Y. Q.; Ning, Z. J.; Zhang, W.; Zheng, W. T.; Yan, Y. F. et al. Trifluoroacetate induced small-grained $CsPbBr_3$ perovskite films result in efficient and stable light-emitting devices. *Nat. Commun.* **2019**, *10*, 665.
[42] Batra, V.; Kotru, S.; Varagas, M.; Ramana, C. V. Optical constants and band gap determination of $Pb_{0.95}La_{0.05}Zr_{0.54}Ti_{0.46}O_3$ thin films using spectroscopic ellipsometry and UV–visible spectroscopy. *Opt. Mater.* **2015**, *49*, 123–128.
[43] Gao, Y. B.; Wu, Y. J.; Lu, H. B.; Chen, C.; Liu, Y.; Bai, X.; Yang, L. L.; Yu, W. W.; Dai, Q. L.; Zhang, Y. $CsPbBr_3$ perovskite nanoparticles as additive for environmentally stable perovskite solar cells with 20.46% efficiency. *Nano Energy* **2019**, *59*, 517–526.

Electronic Supplementary Material

$CsPbBr_3$-DMSO merged perovskite micro-bricks for efficient X-ray detection

Tongyu Shi[1,2,§], Wenjun Liu[1,3,§], Jiongtao Zhu[1], Xiongsheng Fan[1], Zhengyu Zhang[1], Xingchen He[1], Rui He[1], Jiahong Wang[1,2], Kezhen Chen[1,2], Yongshuai Ge[1,2], Xiangming Sun[4], Yanliang Liu[1,2] (✉), Paul K. Chu[5], and Xue-Feng Yu[1,2] (✉)

[1] *Shenzhen Institute of Advanced Technology, Chinese Academy of Sciences, Shenzhen 518055, China*
[2] *University of Chinese Academy of Sciences, Beijing 100049, China*
[3] *Nano Science and Technology Institute, University of Science and Technology of China, Suzhou 215123, China*
[4] *Key Laboratory of Quark and Lepton Physics (MOE), Central China Normal University, Wuhan 430079, China*
[5] *Department of Physics, Department of Materials Science and Engineering, and Department of Biomedical Engineering, City University of Hong Kong, Hong Kong 999077, China*
[§] *Tongyu Shi and Wenjun Liu contributed equally to this work.*

Supporting information to https://doi.org/10.1007/s12274-023-5487-3

Address correspondence to Yanliang Liu, yl.liu4@siat.ac.cn; Xue-Feng Yu, xf.yu@siat.ac.cn

Characterization

The morphology of the $CsPbBr_3$ powder and wafer was examined by scanning electron microscopy (SEM, Zeiss GeminiSEM 300) and atomic force microscopy (Bruker, USA). The chemical structure of the powder were determined by Fourier-transform infrared spectroscopy (FT-IR, Thermo Scientific, Nicolet iS50) according to the KBr pellet method. Powder X-ray diffraction (XRD) was performed on the Rigaku Smartlab 3kW X-ray diffractometer with Cu K_α radiation (λ = 1.54056 Å, 40 kV, 30 mA, 10° min^{-1} from 10 to 60°) and the UV–vis absorption spectra were obtained on a UV–vis spectrometer (UV-1800, Shimadzu). Raman scattering was conducted on the Horiba Jobin Yvon LabRam HR-VIS high-resolution confocal Raman microscope equipped with a 633 nm laser. The PL and TRPL properties were determined using a fluorescent spectrophotometer (Hitachi F-4600 and Edinburgh FLS-1000) at an excitation wavelength at 365 nm. The XPS measurements were carried out on an ESCALAB 250Xi spectrometer (Thermo Scientific, USA) equipped with a pass energy of 30 eV with a power of 100 W (10 kV and 10 mA) and a mono-chromatized AlKα X-ray (hν=1486.65 eV) source. Ultraviolet photoemission spectroscopy (UPS) was performed on an ESCALAB 250Xi electron spectrometer (Thermo Fisher Scientific) using a monochromatic Al Kα source (300 W). UPS was carried out under a pressure of about 2×10^{-10} Pa using helium Iα (21.22 eV) radiation from a discharge lamp operated at 90 W, a pass energy of 1 eV, and a channel width of 25 meV, and the energy resolution was 0.02 eV. A −10 V bias was applied to the samples, in order to separate the sample and analyze low-kinetic-energy cutoffs.

Device characterization

The X-ray detection characteristics were evaluated using an X-ray generation system for medical imaging (Varex, G242, 18932-M8, USA). The accelerating voltage was 50 kV and the currents were varied from 10 to 200 uA. The dose rate of the X-rays was calibrated by the X2 CT dosimeter (Unfors Raysafe, Sweden). During the measurement conducted in darkness, the external electrical bias and current were

recorded by the PDA FS380 semiconductor analyzer. The X-ray imaging capability of the detector was demonstrated by moving the object between the detector (1 mm^2) and X-ray beam (1620 $\mu Gy_{air}\ s^{-1}$) using a self-assembled x-y scanning system consisting of a motorized linear displacement stage (Newport, M-IMS400CC). A motorized linear displacement stage and motion controller (Newport, M-IMS400CC) were used to control scanning along the x and y axes.

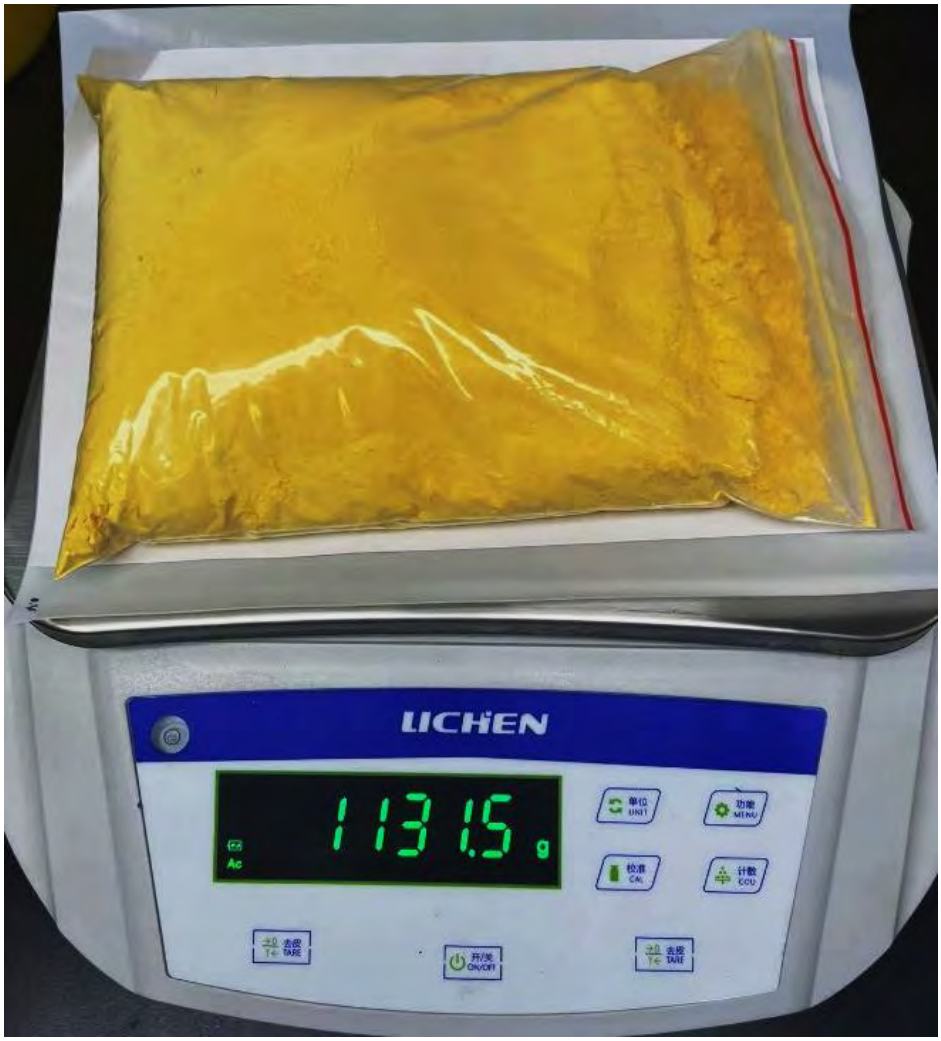

Figure S1. $CsPbBr_3$ powder synthesized by mechanical grinding.

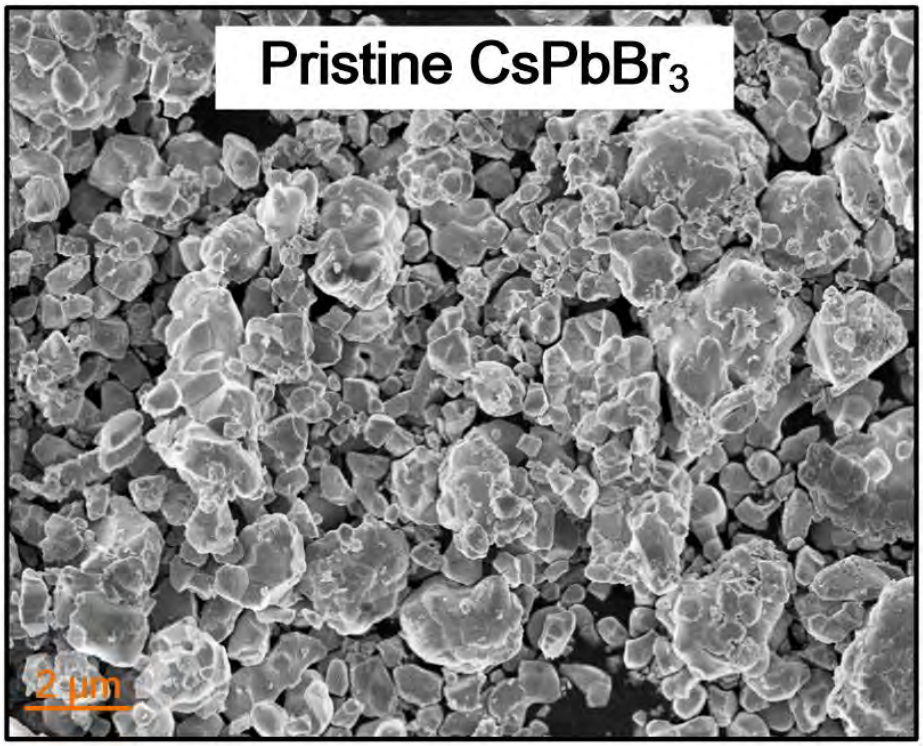

Figure S2. SEM image of the pristine $CsPbBr_3$ powder.

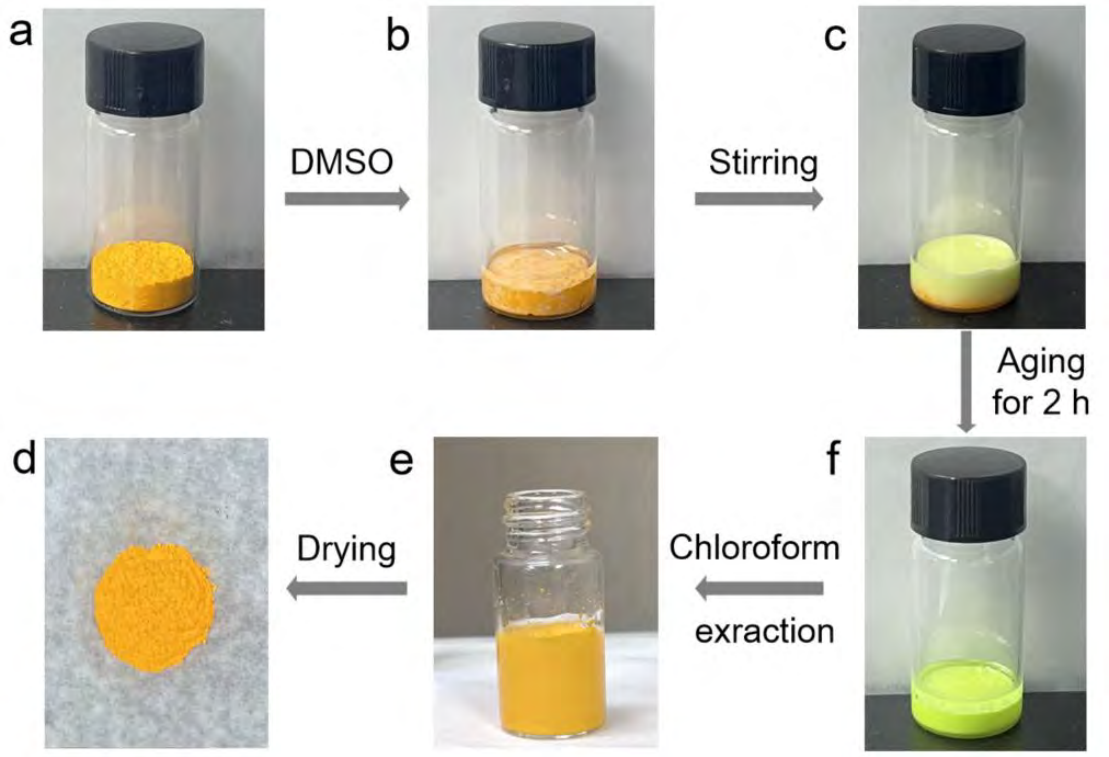

Figure S3. Schematic illustration of preparation of $CsPbBr_3$ in DMSO.

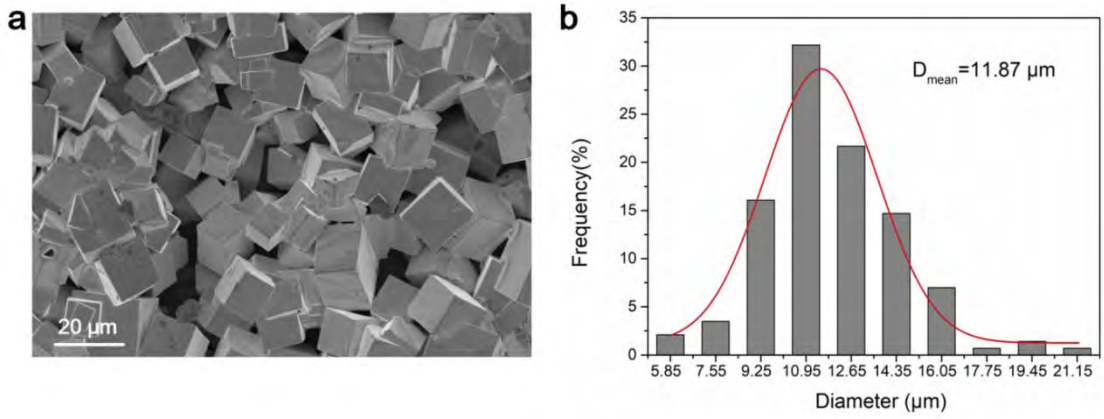

Figure S4. (a) SEM image of $CsPbBr_3$ microbricks and **(b)** particle size distribution histogram).

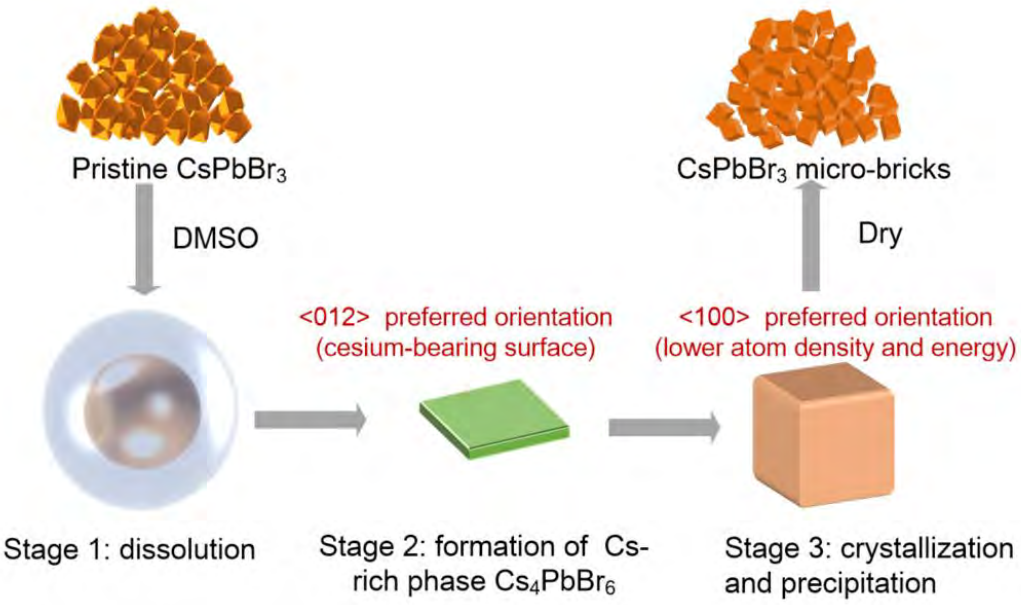

Figure S5. Mechanism proposed for the formation of $CsPbBr_3$ micro-bricks.

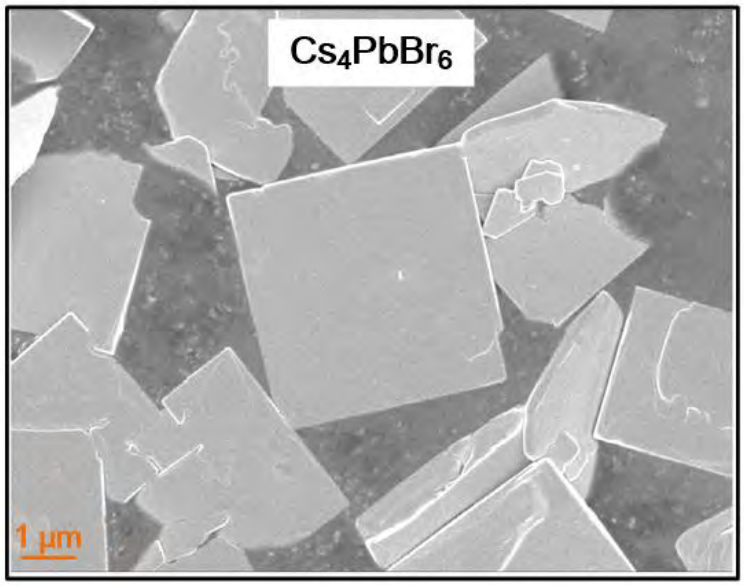

Figure S6. SEM image of the cultivated Cs_4PbBr_6.

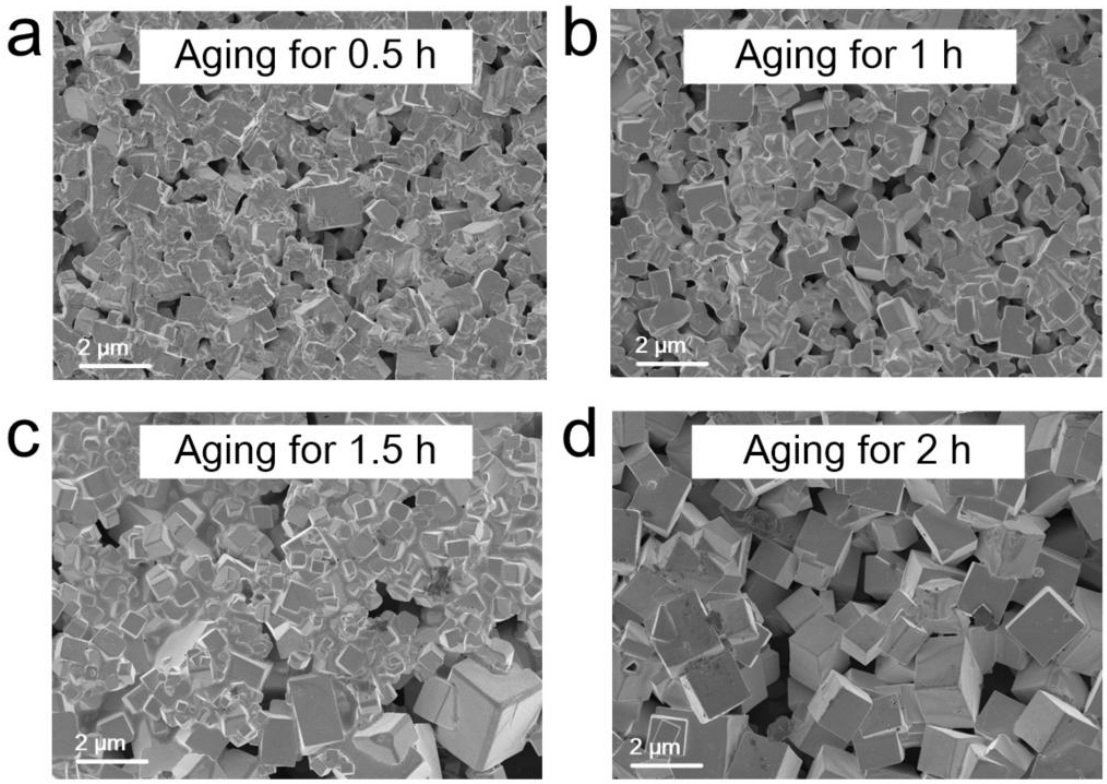

Figure S7. SEM images of the $CsPbBr_3$ obtained at different aging time (from 0.5 h to 2 h).

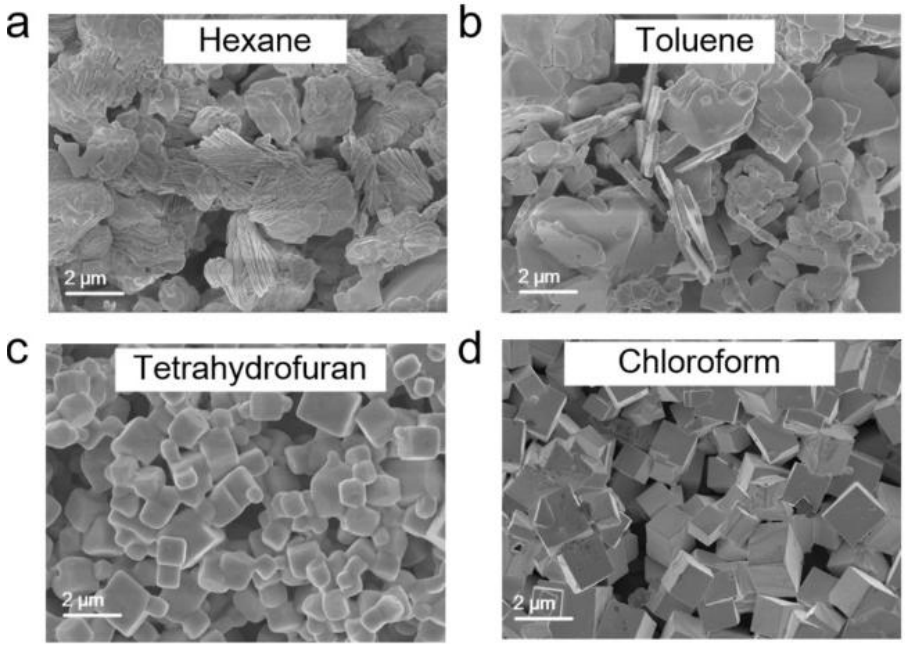

Figure S8. SEM images of the $CsPbBr_3$ obtained from the reactions carried out in different solvent (hexane, toluene, tetrahydrofuran, and chloroform).

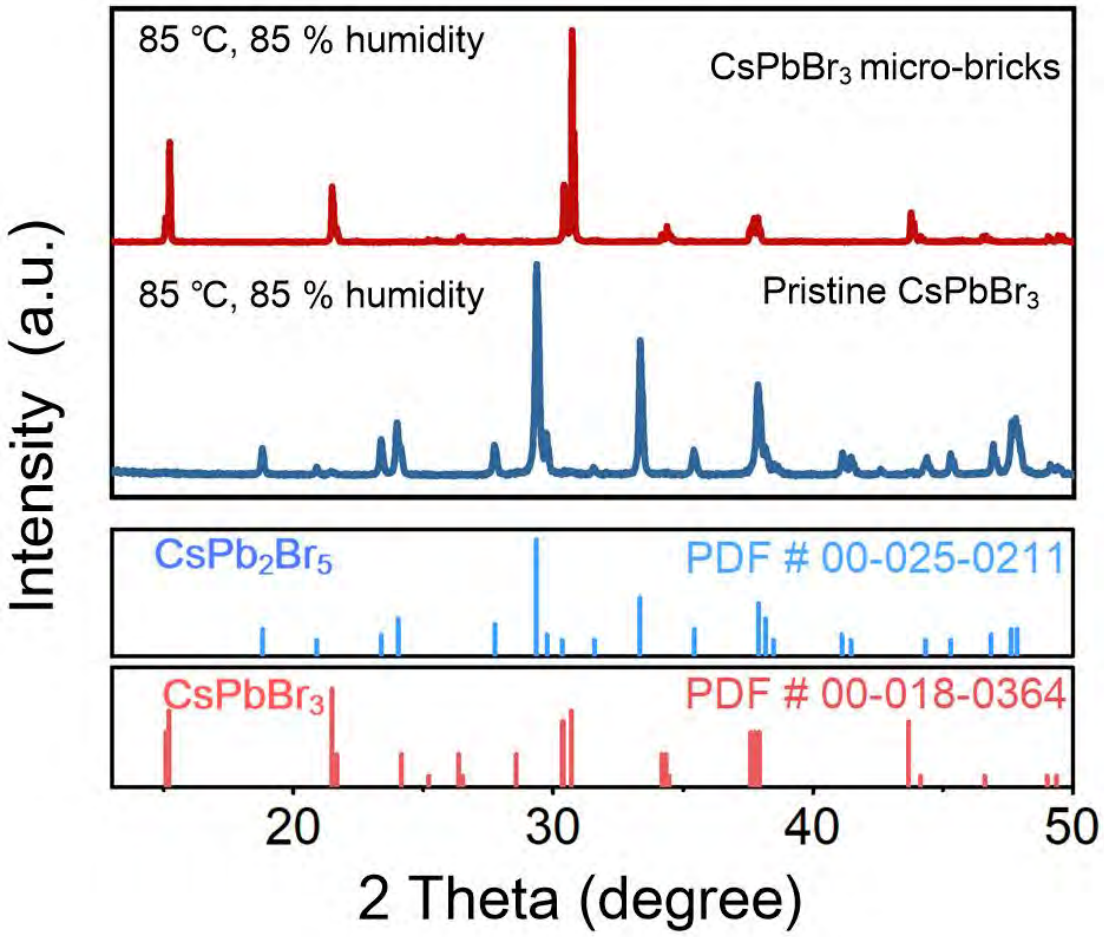

Figure S9. XRD patterns of pristine $CsPbBr_3$ and $CsPbBr_3$ micro-bricks after 21 days of aging under 85 °C and 85% relative humidity.

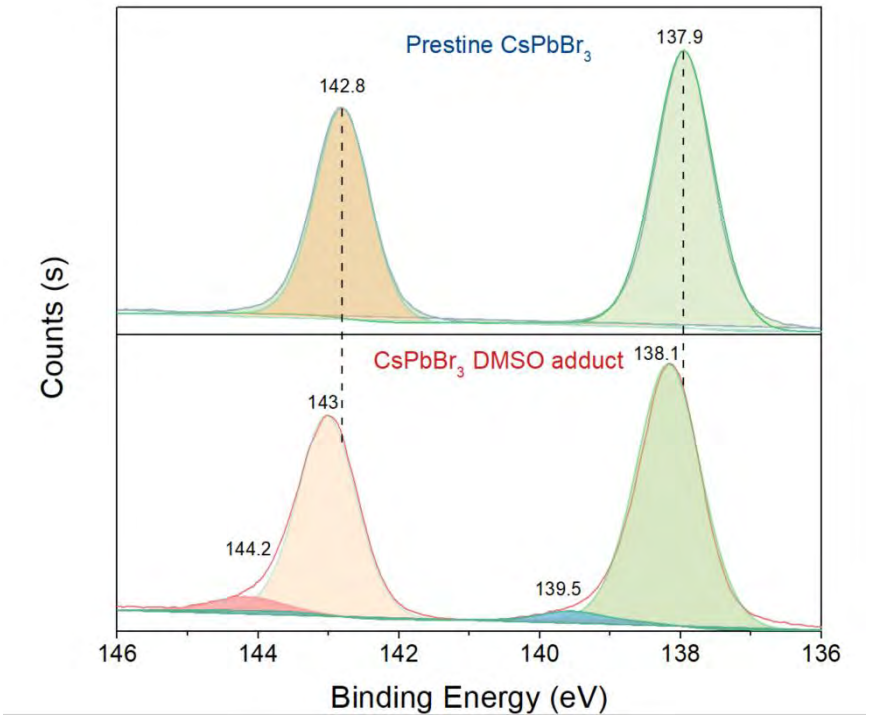

Figure S10. High-resolution Pb 4f spectra of pristine $CsPbBr_3$ and $CsPbBr_3$-DMSO adduct.

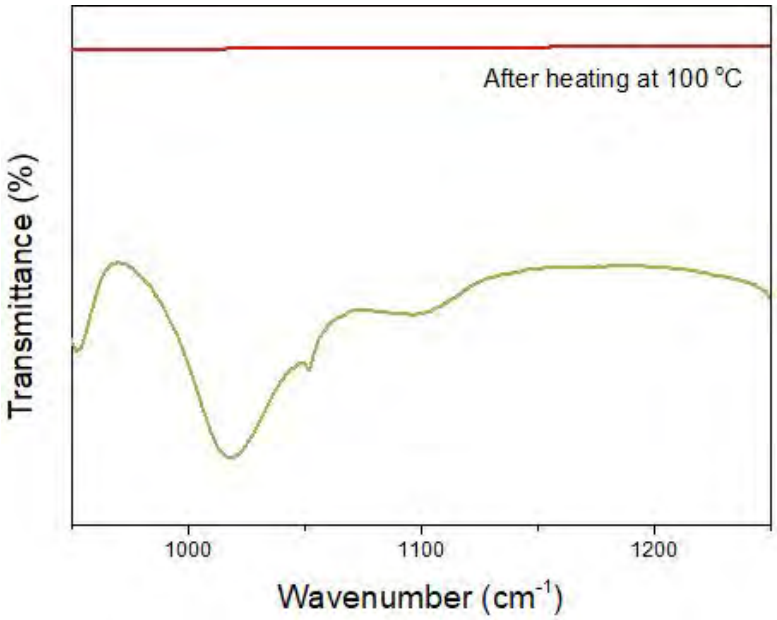

Figure S11. FTIR spectra of the $CsPbBr_3$ micro-bricks after heating at 100 ℃.

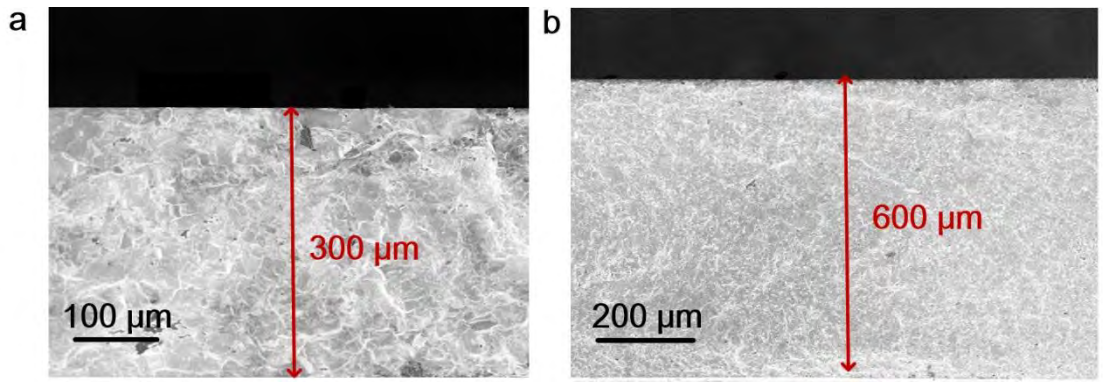

Figure S12. Cross-section SEM images of $CsPbBr_3$ micro-bricks wafer.

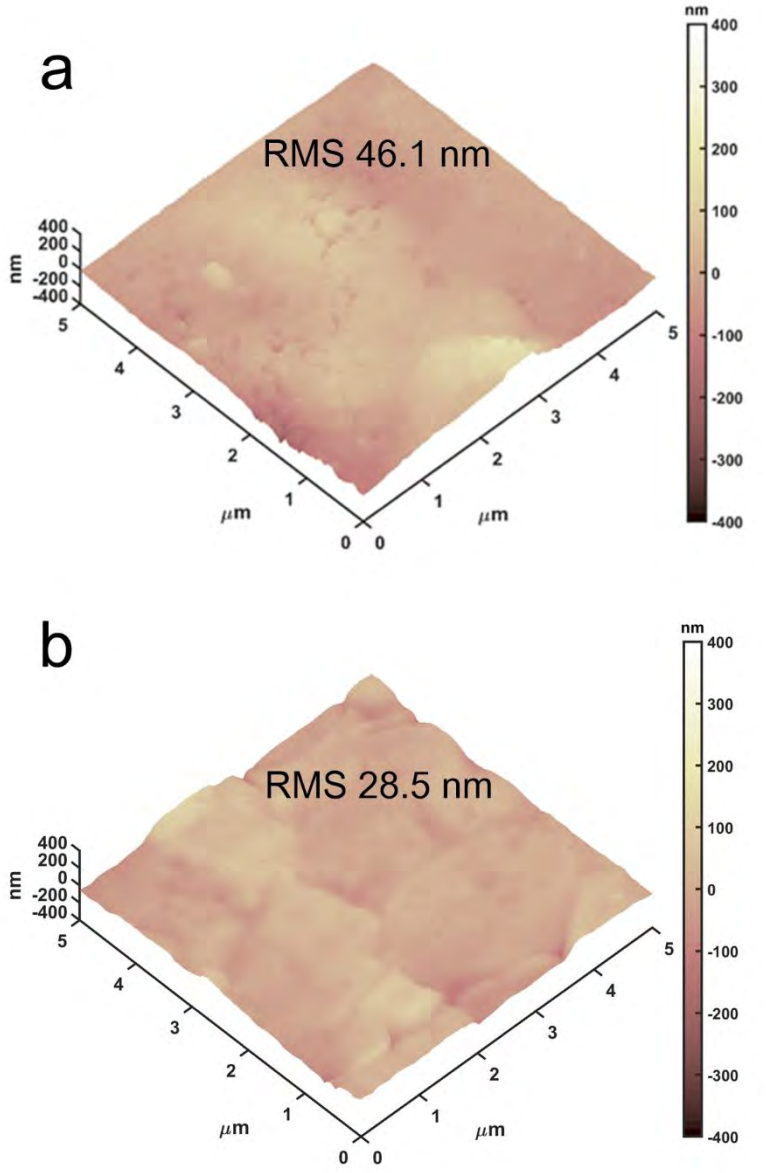

Figure S13. AFM images: (a) pristine $CsPbBr_3$ and (b) $CsPbBr_3$ micro-bricks wafers.

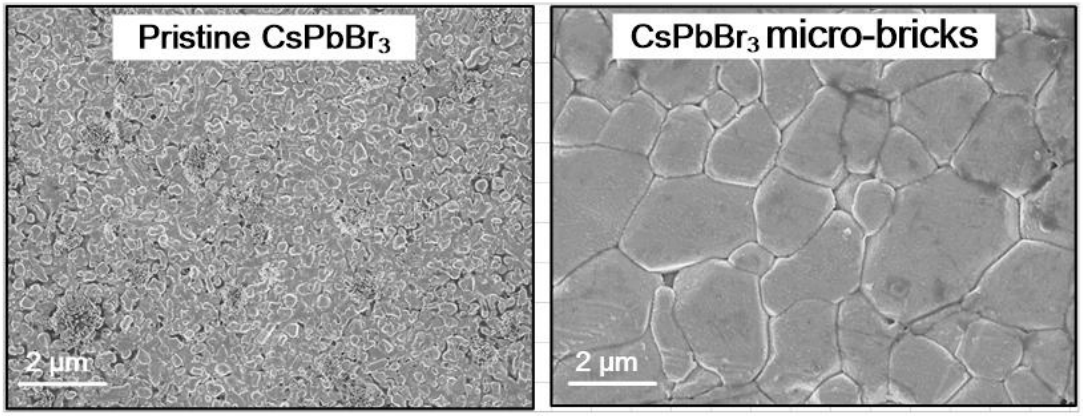

Figure S14. SEM images of pristine $CsPbBr_3$ and$CsPbBr_3$ micro-bricks wafers after 14 days under 25 °C and 60% relative humidity.

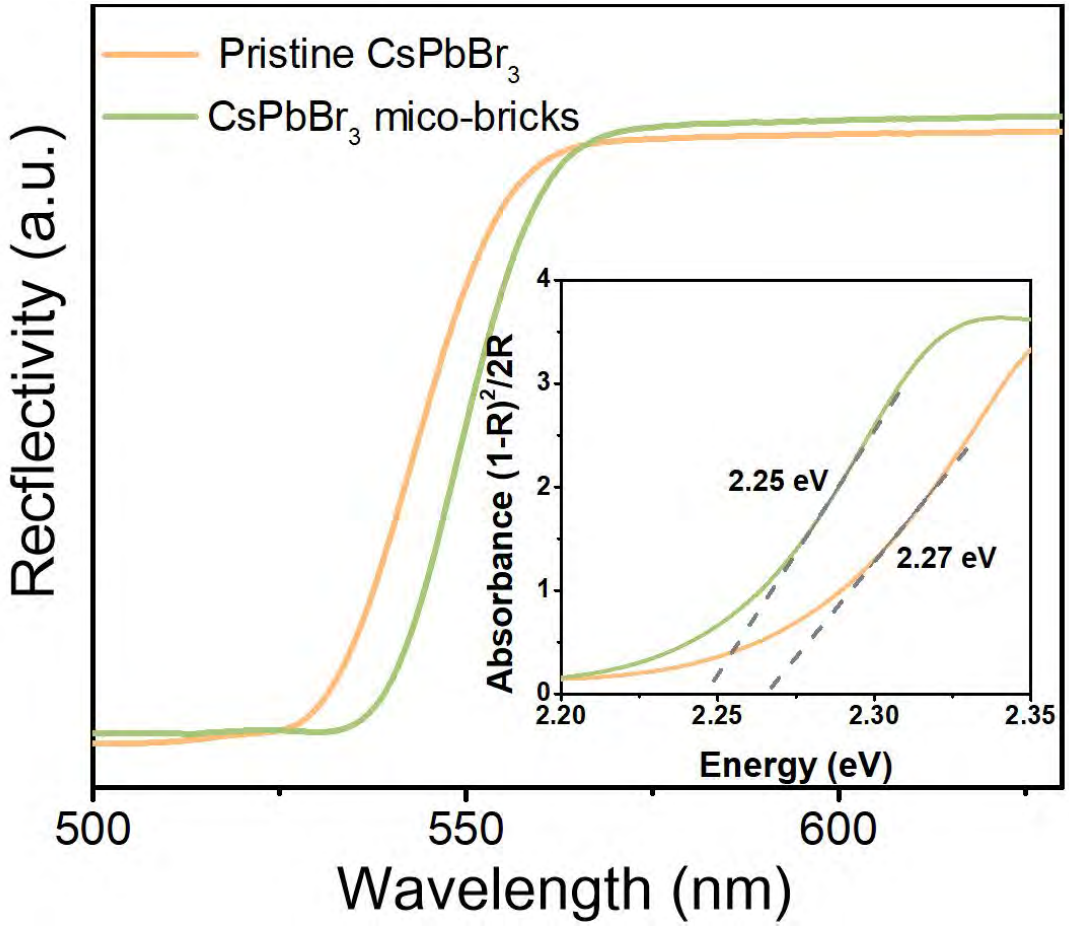

Figure S15. UV-vis spectra of the pristine $CsPbBr_3$ and $CsPbBr_3$ micro-bricks (inset showing the Tauc plot).

Table S1. Fitting parameters and average lifetime of the wafers

	A_1	τ_1 [ns]	A_2	τ_2 [ns]	T_{avg}
Pristine $CsPbBr_3$	4276.50778	11.74227	24009.86006	2.29315	6.800394059
$CsPbBr_3$ micro-bricks	4042.45622	33.07301	8278.46088	5.70064	25.93176172

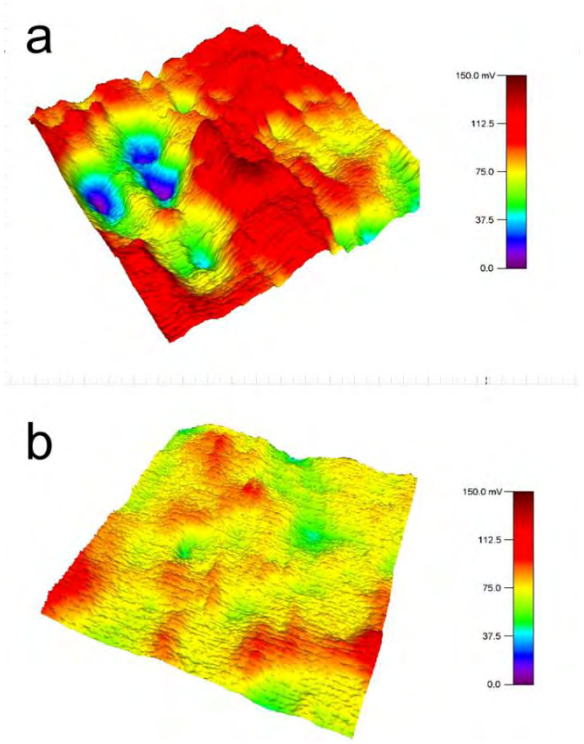

Figure S16. KPFM images of (a) pristine $CsPbBr_3$ and (b) $CsPbBr_3$ micro-bricks wafers.

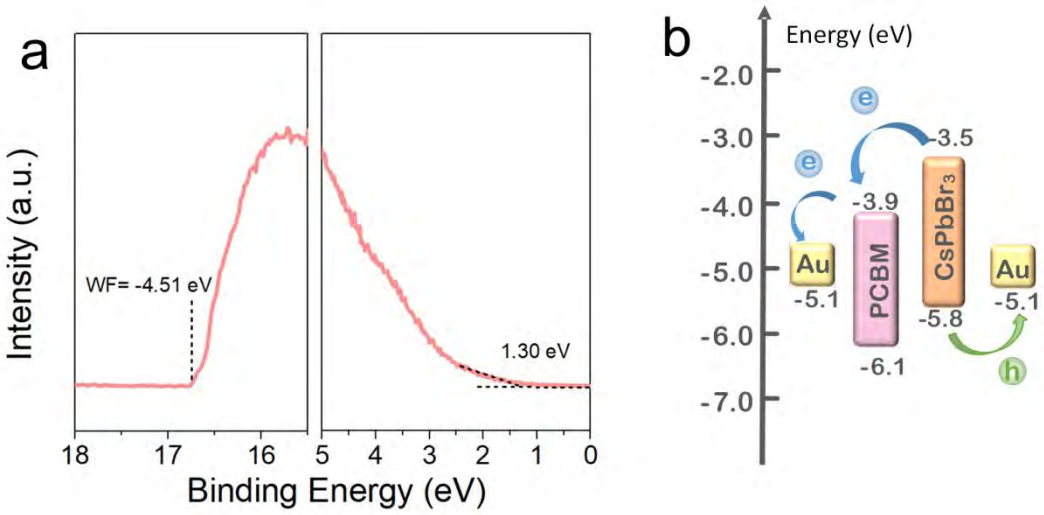

Figure S17. UPS spectra and energy level diagram of perovskite X-ray detector.

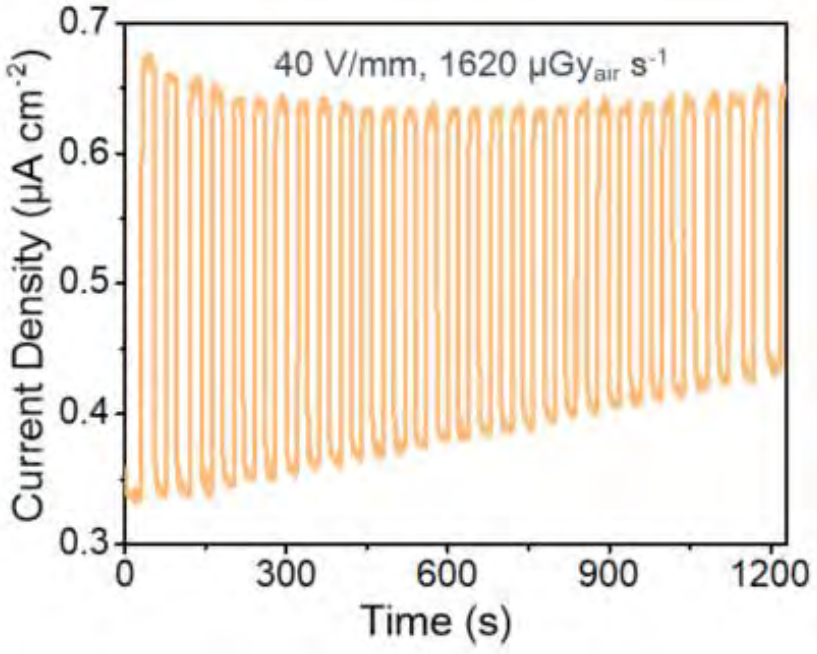

Figure S18. Stability of the pristine $CsPbBr_3$ detector under pulsed X-ray irradiation at a fixed dose rate.

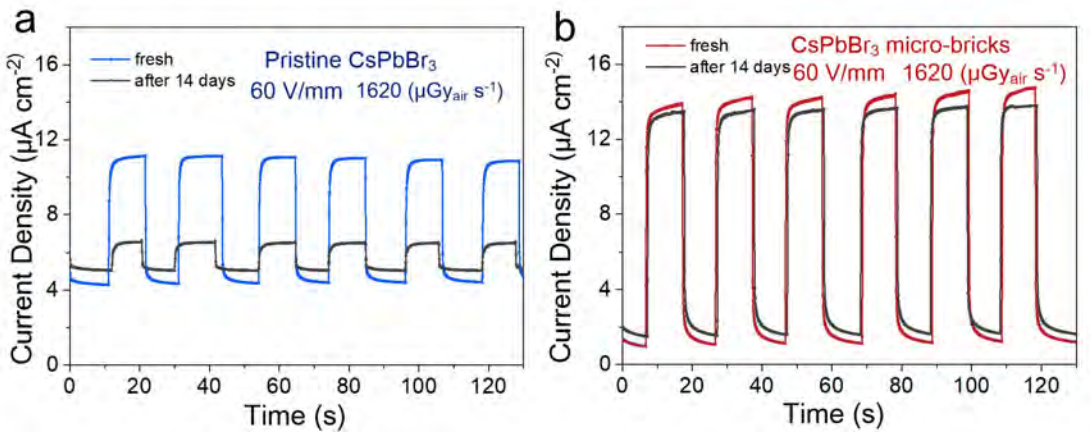

Figure S19. The storage stability of (a) pristine $CsPbBr_3$ and (b) $CsPbBr_3$ micro-bricks detector in ambient condition (25 ℃, relative humidity 60%).